PHYSICS

Holographic imaging of electromagnetic fields via electron-light quantum interference

I. Madan[1]*, G. M. Vanacore[1]*, E. Pomarico[1], G. Berruto[1], R. J. Lamb[2], D. McGrouther[2], T. T. A. Lummen[1]†, T. Latychevskaia[1], F. J. García de Abajo[3,4], F. Carbone[1]‡

Copyright © 2019 The Authors, some rights reserved; exclusive licensee American Association for the Advancement of Science. No claim to original U.S. Government Works. Distributed under a Creative Commons Attribution NonCommercial License 4.0 (CC BY-NC).

Holography relies on the interference between a known reference and a signal of interest to reconstruct both the amplitude and the phase of that signal. With electrons, the extension of holography to the ultrafast time domain remains a challenge, although it would yield the highest possible combined spatiotemporal resolution. Here, we show that holograms of local electromagnetic fields can be obtained with combined attosecond/nanometer resolution in an ultrafast transmission electron microscope (UEM). Unlike conventional holography, where signal and reference are spatially separated and then recombined to interfere, our method relies on electromagnetic fields to split an electron wave function in a quantum coherent superposition of different energy states. In the image plane, spatial modulation of the electron energy distribution reflects the phase relation between reference and signal fields. Beyond imaging applications, this approach allows implementing quantum measurements in parallel, providing an efficient and versatile tool for electron quantum optics.

INTRODUCTION

Holography allows capturing both the phase and the amplitude of a signal distribution by superimposing it with a known reference. This idea was originally proposed by Gabor (*1*, *2*) to improve the resolution of an electron microscope. He first demonstrated the principle using light optics, while holography with electrons was shown shortly afterward (*3*). With the invention of intense coherent light sources (lasers) and their most recent technological advancements, optical holography has become a popular technique for three-dimensional (3D) imaging of macroscopic objects, security applications (*4*, *5*), and microscopic imaging (*6*). Electron holography (*7*, *8*) has been successfully used in materials science (*9*) and also to image electrostatic potentials (*10*, *11*) and magnetic structures (*12*). More generally, the holography principle can be extended to any kind of detection configuration involving a periodic signal capable of undergoing interference, such as sound waves (*13*), x-rays (*14*), or femtosecond pulse waveforms (spectral holography) (*15*).

Various recent experiments have been implemented to extend the concept of holography from a static imaging method to a dynamical probe, capable of recording the temporal evolution of both the amplitude and the phase of a signal. Time-resolved optical holography has been successfully realized in the femtosecond regime (*16*, *17*) and further used in combination with photoemission for plasmon imaging with enhanced spatial resolution in time-resolved photoemission electron microscopy (tr-PEEM) (*18*, *19*).

The introduction of temporal resolution in electron holography is more challenging, and so far, the adopted schemes use temporal gating working in the microsecond time scale (*20*, *21*). Reaching the ultrafast domain could become a reality owing to recent developments in the ultrafast transmission electron microscope (UEM), in which femtosecond lasers are used to create ultrafast electron pulses (*22*, *23*). Those developments have enabled real-time filming of electronic collective modes (*24*–*26*), strain fields (*27*), and magnetic textures (*28*, *29*) with a temporal resolution down to a few hundred femtoseconds. Holography with ultrafast electron pulses should also be attainable (*23*, *30*), yielding similar time resolution and allowing subpicosecond imaging of magnetic and electric fields to be performed. However, most applications of interest involve spatially resolved phase dynamics of electromagnetic fields on the time scale of one to a few femtoseconds. These include electronic excitations in condensed matter, nonradiative energy transfer in molecules, and excitonic currents and condensates, as well as optical fields in metamaterials and photonic crystals.

Here, we demonstrate a time-domain holographic imaging technique implemented in UEM and based on the quantum coherent interaction of electron wave packets with multiple optical fields. We illustrate this method by capturing attosecond/nanometer-resolved phase-sensitive movies of rapidly evolving local electromagnetic fields in plasmonic structures, which serve as an example of nanoscale imaging of phase dynamics. We implement two experimental configurations. The first and simplest one relies on using electron pulses to map the optical interference between a polaritonic reference and a polaritonic signal, both excited with ultrashort light pulses, which is similar to near-field optical or tr-PEEM instruments. The second implementation, which is conceptually different and unique to UEM, is based on Ramsey-type interference (*31*) and relies on the coherent modulation of the electron wave function by means of spatially separated reference and signal electromagnetic fields. Because the interaction with the sequence of optical fields occurs along the electron propagation direction, the constraint imposed by high transverse electron coherence, necessary for conventional electron holography, is now removed. This limitation has so far prevented the practical realization of holography in time-resolved experiments using pulsed electrons, particularly because multielectron pulses necessary for imaging applications have degraded coherence. Besides the obvious implications for the investigation of ultrafast coherent processes at the nanometer

[1]Institute of Physics, Laboratory for Ultrafast Microscopy and Electron Scattering (LUMES), École Polytechnique Fédérale de Lausanne, Station 6, CH-1015 Lausanne, Switzerland. [2]SUPA, School of Physics and Astronomy, University of Glasgow, Glasgow G12 8QQ, UK. [3]ICFO–Institut de Ciencies Fotoniques, The Barcelona Institute of Science and Technology, 08860 Castelldefels, Barcelona, Spain. [4]ICREA–Institució Catalana de Recerca i Estudis Avançats, Passeig Lluís Companys 23, 08010 Barcelona, Spain.
*These authors contributed equally to this work.
†Present address: Single Cell Facility, Department of Biosystems Science and Engineering (D-BSSE), ETH Zürich, Mattenstrasse 26, 4058 Basel, Switzerland.
‡Corresponding author. Email: fabrizio.carbone@epfl.ch

length scale, we show that our approach could be used for accessing the quantum coherence of generic electronic states in a parallel fashion, which can be relevant for future electron quantum optics applications.

RESULTS AND DISCUSSION

Conventional and holographic photon-induced near-field electron microscopy imaging

A simple implementation of holographic UEM is based on local interference of two fields, which, in the present study, we realize using two propagating surface plasmon polaritons (SPPs). We first describe the interaction mechanism of the electron pulse with a single SPP (Fig. 1A) and then examine the holograms produced by interference between the two SPPs (Fig. 1B).

In conventional photon-induced near-field electron microscopy (PINEM) (*24*), electrons inelastically absorb or emit photon energy quanta $\hbar\omega$ (1.57 eV in our experiment). Filtering the inelastically scattered electrons allows one to form real-space images of the plasmon field (*24*). The time resolution in PINEM is set by the duration τ_{el} of the electron pulses, which restrains the ability to perform real-space dynamical imaging to a few hundred femtoseconds (*23*–*25*). This time scale is in fact roughly two orders of magnitude longer than the plasmon period and even longer than the duration of the plasmon wave packet determined by the 55-fs light pulse duration. While high spatial resolution can be achieved by monitoring plasmonic standing waves (*32*), for a traveling SPP, the electron pulse duration limits spatial resolution to $\Delta x \sim \tau_{el} v_g$, where v_g is the plasmon group velocity. This is schematically shown in Fig. 1A. For the SPPs at the Ag/Si_3N_4 interface studied here, the resulting blurring in the real-space image is typically $\Delta x \sim 50$ μm, which is comparable with the plasmon decay length (~65 μm in our system).

This problem of blurring can be overcome via a holographic approach, which uses a second SPP wave used as a reference, to create an interference pattern with the SPP of interest. This interference forms only when both waves overlap in space and time (Fig. 1B). Denoting $\boldsymbol{k}_1$ and $\boldsymbol{k}_2$ as the wave vectors of the two SPPs, the electric field associated with the interference pattern becomes

$$\begin{aligned}\mathcal{E}_{tot}(\mathbf{r},t) &= \mathcal{E}\cos(\mathbf{k}_1\cdot\mathbf{r}-\omega t)+\mathcal{E}\cos(\mathbf{k}_2\cdot\mathbf{r}-\omega t)\\ &= 2\mathcal{E}\cos((\mathbf{k}_1-\mathbf{k}_2)\cdot\mathbf{r}/2)\cos((\mathbf{k}_1+\mathbf{k}_2)\cdot\mathbf{r}/2-\omega t)\end{aligned} \quad (1)$$

Here, we consider only the component of the electric field that contributes to the interaction, namely, the one parallel to the electron momentum (*33*). The final response is defined by the integral of the field amplitude over the electron pulse duration. As our optical pulses comprise ~35 oscillation periods (4σ pulse duration), the amplitude of the oscillatory component averages out over the time, thus reducing the contribution of the rightmost cosine factor of Eq. 1 to a constant factor in the inelastic intensity, eliminating spatial oscillations with $\mathbf{k}_1 + \mathbf{k}_2$ and leaving only those with $\mathbf{k}_1 - \mathbf{k}_2$. The resulting energy-filtered image is thus a hologram with interference fringes of period $2\pi/|\mathbf{k}_1 - \mathbf{k}_2|$ (see Fig. 1B).

When the SPPs are launched by independent pulses, one can tune the relative delay between the reference and the field of interest with subcycle precision (330 as in this work), therefore obtaining the real-space evolution of the phase of the electric field. Moreover, the finite duration of the reference pulse provides a temporal gate, effectively improving the temporal resolution of PINEM in tracking group velocities down to the duration of the laser pulse, in our case, 55 fs. A similar concept has been presented in (*34*) to control the temporal profile of the electron pulse using a sequence of two incoherent interactions with a visible and near-infrared (IR) pulses, whereas here, the adoption of two phase-locked light pulses provides a fundamentally higher signal-to-background ratio (up to 100%) and gives direct access to the phase dynamics.

To demonstrate the holographic PINEM concept, we have implemented the experiment described in Fig. 1B using a nanostructure composed of two perpendicular slits, fabricated by Ga ion milling of a 43-nm-thick Ag film deposited on a Si_3N_4 membrane (Fig. 1, inset). Each slit radiates SPPs at the interface between Ag and Si_3N_4 when excited with light polarized normally to its long edge (see Materials and Methods for more details). The experiment is conducted under a critical angle condition (*35*) that minimizes the interaction of the electron with the light beam interrupted by the film (see Materials and Methods).

In Fig. 2, we show the holograms formed by the two SPPs with relative pulse delays of −77, −20, 0, and 22 fs. These real-space images of the plasmonic field are obtained by energy-filtering inelastically scattered electrons (see Materials and Methods) (*33*, *36*). By varying the delay between the two light pulses, the position of these interference patterns changes across the square area delimited by the two slits, moving from the left-bottom part at negative times to the top-right region for positive delays (see also movies S1 and S2). This demonstrates the gating effect of the reference pulse, showing that the envelope of the interference pattern is defined by the optical and not by the electron pulse duration. The intensity profiles at each time delay plotted along the $\mathbf{k}_1 - \mathbf{k}_2$ direction (marked by the arrow in Fig. 2A) are shown in Fig. 2 (E to H).

Access to the phase dynamics allows us to measure the phase velocity v_p (see Fig. 2I and movie S2), while the improved temporal resolution of this method enables the determination of the group velocity v_g (Fig. 2J and movie S1). By taking into account the geometrical arrangements of the beams and the slits (see Materials and Methods

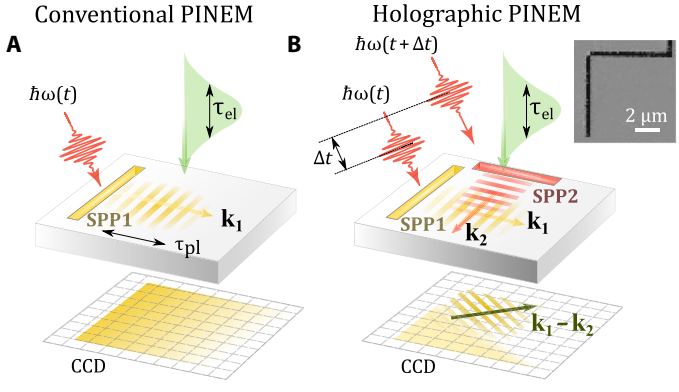

Fig. 1. Conventional versus holographic PINEM imaging. (**A**) In conventional PINEM, propagating SPPs are imaged with long electron pulses, rendering only its time-averaged envelope with a spatial resolution $\Delta x \sim \tau_{el} v_g$. (**B**) In local holographic PINEM, two SPPs propagate with orthogonal wave vectors $\mathbf{k}_1$ and $\mathbf{k}_2$ forming a standing wave pattern along the direction $\mathbf{k}_1 - \mathbf{k}_2$, which is imaged as a periodic modulation in PINEM (the hologram). The interference contrast appears only when the two pulses overlap in space and time. Inset: SEM image of a fabricated structure. Black regions are grooves, which serve as plasmon sources. CCD, charge-coupled device.

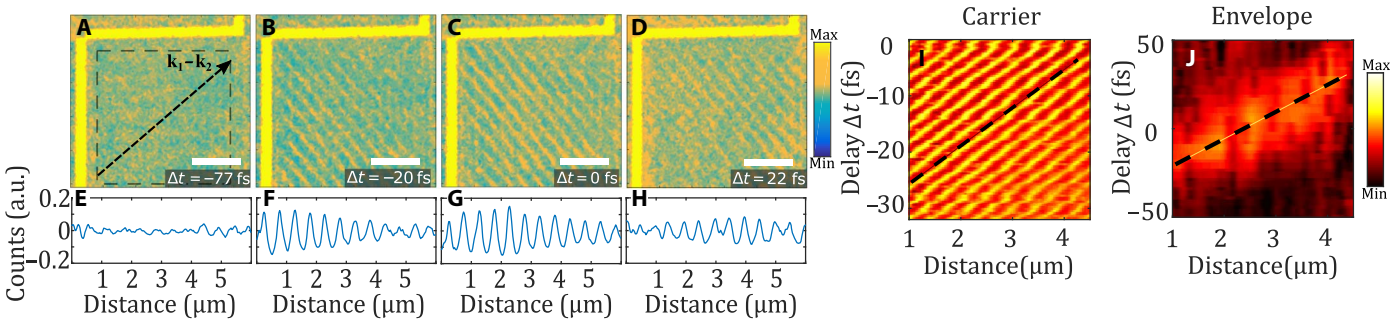

Fig. 2. Holographic images formed by two pulses of orthogonal polarization at different delays. (**A** to **D**) Micrographs of PINEM images for different values of the relative time delay Δt between the photo-exciting pulses, as indicated in each image. Scale bars, 2 μm. The SPP emitted from the vertical slit propagates from left to right. Correspondingly, the interference pattern moves from the bottom-left to the top-right corner. (**E** to **H**) Modulation of the electron counts along the $\mathbf{k}_1 - \mathbf{k}_2$ direction indicated in (A), calculated as the average of counts along the direction orthogonal to $\mathbf{k}_1 - \mathbf{k}_2$, taken within the dashed square indicated in (A). (**I**) Evolution of the profiles shown in (E) to (H) as a function of delay between the two pulses; because of the experimentally adopted sample orientation, retardation effects cause the slope of the fringes (see dashed line as a guide) to be decreased by a factor of 0.71 with respect to the SPP phase velocity (see Materials and Methods). (**J**) Envelope of the interference pattern as a function of delay between the two pulses, with the slope of the peak (see dashed line as a guide) also decreased by a factor of 0.71 with respect to the SPP group velocity. Envelope data have been acquired in a separate measurement over a longer delay span and with larger time steps. a.u., arbitrary units.

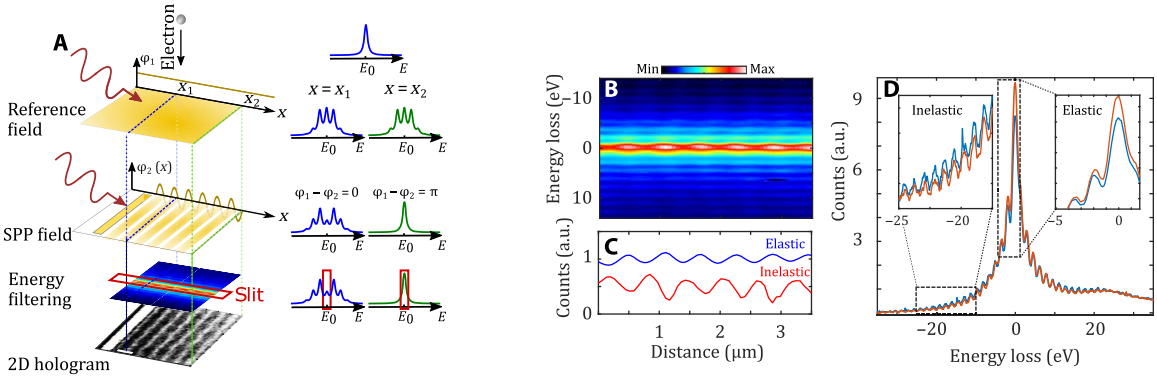

Fig. 3. Principle of spatially separated electron holography. (**A**) The initial energy distribution of the electron beam is a function of energy that is singly peaked at $E = E_0$ (right). Interaction with the reference field produces coherent superposition states with energies $E = E_0 \pm n\hbar\omega$. The ensuing interaction with an SPP depends on the relative phase between SPP and reference fields, which results in a position-dependent electron energy distribution. The elastic part of the electron spectrum is then used to form the 2D hologram. The spectra on the right are simulations from an analytical model (see Materials and Methods). (**B**) Hybrid energy-space map (spectrogram) of the electrons after interaction with the two fields, as schematized in (A). (**C**) Spatial profiles of the normalized intensity for elastic (blue curve) and inelastic (red curve) electrons, as obtained from (B) by energy-averaging from −1 to 1 eV for the elastic contribution and from −27 to −12 eV for the inelastic one. (**D**) Energy profiles at the maximum and minimum of the spatial modulation shown in (B), averaged over four periods.

and note S1), we obtain $v_p = 2.69 \pm 0.05 \times 10^8$ m/s and $v_g = 1.95 \pm 0.07 \times 10^8$ m/s, which agree well with the estimated theoretical values of $v_p = 2.64 \times 10^8$ m/s and $v_g = 2.04 \times 10^8$ m/s, respectively. Because our technique is essentially a spatially resolved temporal cross-correlation method, the characterization of the wave package cross-correlation can be performed with arbitrary precision, in our case, 330 as.

Spatially separated quantum holography

The holographic approach presented above can be greatly generalized using the coherence between the different energy states of the quantum ladder in which the electronic wave function is split upon interacting with light (*35*, *37*, *38*). This method exploits the fact that the electrons carry information about the amplitude and the phase of the optical field even after the interaction is finished. Thus, the result of any ensuing interaction of the electron will depend on the relative phase between the initial and subsequent optical fields (*31*). This allows us to separate in space the interfering fields, enabling in turn the adoption of more practical reference fields.

In particular, we make use of a semi-infinite light field created by the reflection of the optical beam from an electron-transparent optical mirror (Fig. 3A). The interrupted optical field interacts with the electrons via the inverse transition radiation effect (*35*, *39*), therefore creating a material-independent reference field, with nearly constant spatial amplitude and phase, providing an optimum reference for holography.

The interaction with this first optical field is captured in the spatially homogeneous coupling factor β_1, which is a complex number uniquely determined by the amplitude and the phase of the optical field, as well as the electron trajectory (*33*). The interaction with the spatially varying signal field, occurring at a distance d further down the electron path, is captured by a space-dependent coupling factor $\beta_2(x, y)$. The total interaction is given by a simple sum of two complex numbers $\beta(x, y) = \beta_1 + \beta_2(x, y)$. The final energy distribution is determined by the modulus $|\beta(x, y)|$ (*33*, *40*), which for slowly decaying plasmon fields is predominantly determined by the spatially dependent phase difference $\Delta\varphi(x, y)$ between the two optical fields.

In Fig. 3 (B to D), we show the experimentally measured variation of the electron energy distribution as a function of the distance of an electron beam from a directional plasmon emitter, formed as a result of the above-described spatially separated interference. The distribution has the periodicity of the plasmon wavelength, in both the elastic and inelastic channels, which have opposite phases [see Fig. 3C, where we plot the energy profile corresponding to the maximum (red) and minimum (blue) of the elastic peak, which correspond to $\Delta\varphi = \pi$ and 0, respectively].

The interaction strength β depends on the electric field amplitude linearly as

$$\beta(x,y) = \frac{e}{\hbar\omega}\int_{-\infty}^{\infty} e^{-\frac{i\omega z}{v}}\mathcal{E}_1(z)e^{-i\phi_1}\mathrm{d}z + \frac{e}{\hbar\omega}e^{-\frac{i\omega d}{v}}\int_{-\infty}^{\infty} e^{-\frac{i\omega z}{v}}\mathcal{E}_2(x,y,z)e^{-i\phi_2(x,y)}\mathrm{d}z$$

Here, $\mathcal{E}_1$, φ_1 and $\mathcal{E}_2$, φ_2 are amplitudes and phases of the reference and signal fields, respectively, e and $\hbar$ are fundamental constants, and v is the electron velocity. The linearity of this formula implies that the nonlocal interference contrast is mathematically equivalent to the previously discussed case of local interference. The only difference is a constant phase offset $e^{-i\omega d/v}$ between the two fields, which can be compensated by properly choosing the mutual delay between them. For fields that substantially vary not only within the (x, y) plane but also along the z coordinate (3D nano-objects, nonplanar plasmonic structures, etc.), the phase factor $e^{-i\omega d/v}$ produces an important contribution to the overall contrast. It reflects the change in the phase of the signal field due to retardation. In other words, it contains information about the z distribution of the signal field, which can be directly retrieved because both the electron velocity and the light frequency are known quantities. This would allow for a complete 3D phase tomography of the signal of interest to be performed and could be used to reconstruct the complex electric field distribution around 3D particles or nanostructures.

The mathematical equivalence of local plasmon holography and spatially separated quantum holography allows us to treat the recorded holograms with the same formalism of propagating and standing waves. In the spatially separated realization, the homogeneous reference field is noncollinear with respect to any propagating signal field, ensuring the formation of a standing wave pattern. An additional phase variation appears if the wavefront of the reference wave is tilted with respect to the mirrors surface, generating Doppler-like shifts (*41*) in the interference pattern.

We present an observation of this effect in Fig. 4. We record holograms formed by the tilted wavefront of the light reflected from a Ag mirror and a plasmon wave emitted from a hole carved in the Ag layer. The tilted wavefront can be described by Eq. 1 through the addition of the small in-plane wave vector component $\mathbf{k}_2 = \mathbf{k}_{ph||}$, coherently superimposing on the in-plane plasmon wave vector $\mathbf{k}_1 = \mathbf{k}_{SPP}$, whose direction is radial with respect to the center of the hole (see Fig. 4A). The resulting pattern exhibits a periodicity $\mathbf{k}_1 - \mathbf{k}_2 = \mathbf{k}_{SPP} - \mathbf{k}_{ph||}$, which is direction dependent and leads to the Doppler effect shown in Fig. 4 (B and D). This effect is naturally absent in the untilted hologram shown in Fig. 4C.

Detection of electronic quantum coherence

Besides the direct implications for the visualization of phase-sensitive dynamics, our holographic approach can be useful for the characterization of the quantum state of a generic free-electron state, such as the one generated in the photoemission process from a solid-state material illuminated with ultraviolet (UV) light. This problem is of great interest not only for UEM but also for free-electron lasers and attosecond physics (*42*). It has been shown that, in the photoemission process, electrons carry information about the phase of the exciting optical field (*43*). However, because of several uncontrolled factors, such as screening potentials, scattering events, or external field inhomogeneities, coherence is usually lost in part (*44*). While, in attosecond science, reliable techniques have been developed to investigate this issue (*45*, *46*), it is still a pending problem in UEM, which is particularly relevant when targeting sub-electronvolt excitations (*26*) in condensed matter, where the relevant energy is smaller than or comparable to the electron energy spread, and thus, beam coherence becomes an important condition.

We stress that the quantum coherence of an electron state, while related, must not be confused with the coherence between the electrons

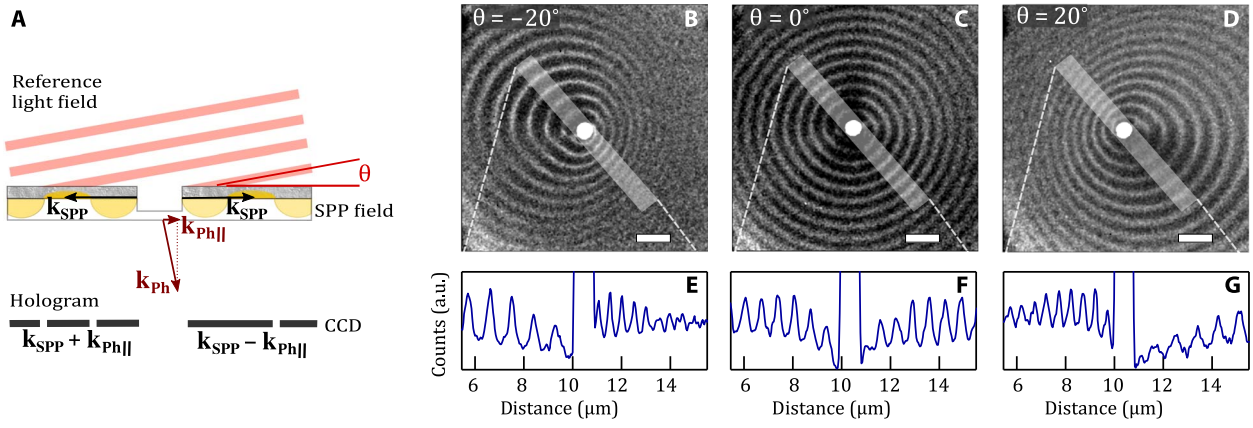

Fig. 4. Doppler effect in spatially separated electron holography. (**A**) Schematics of the experiment. Top: A laser pulse of frequency ω creates both a reference field and a signal field. The reference is produced by reflection from the surface, with an in-plane wave vector dependence on the tilt angle θ given by $k_{ph||} = (\omega/c)\sin\theta$. The signal field is the SPP excited at the metal/dielectric interface, with a tilt-independent in-plane wave vector k_{SPP}. Bottom: Change in the period of the hologram depending on the relative direction of $\mathbf{k}_{ph||}$ and $\mathbf{k}_{SPP}$. (**B** to **D**) Holograms observed for incident angles θ = −20°, 0°, and 20°, respectively. Scale bars, 2 μm. (**E** to **G**) Spatially resolved intensity profiles corresponding to the areas highlighted in white in (B) to (D).

usually discussed in the context of electron holography. In the context of holography, coherence rather refers to a measurement of the monochromaticity and phase stability of the electron plane wave, whereas quantum coherence in the context of the present study describes our ability to determine whether an electron is in a pure state or rather entangled to the environment. In a quantum coherent state, an electron can be in a superposition of states with vastly different energies and, as a consequence, without being very coherent in the holographic sense (i.e., not producing clear sinusoidal interference patterns when subjected to interference experiments). The word coherence in the quantum sense indicates that the phase between different energy states is determined via the time evolution operator and is not random. In mathematical terms, quantum coherences of a state manifest in nonzero off-diagonal terms of its density matrix. In our method, the interaction between the SPP and the electron makes a generic electronic quantum state ρ_{in} evolve unitarily into a space-dependent (distance x) state $\rho_{out}(x)$. In this manner, off-diagonal terms of ρ_{in} get projected onto the observable diagonal terms of $\rho_{out}(x)$. As our approach is able to simultaneously record spatial and spectral information (see Fig. 3B), we can readily determine how the energy distribution of the final electronic state varies with respect to x. This information can be used to identify and characterize the quantum coherences of the initial state.

The model calculation presented in Fig. 5 shows how our method can discriminate between a highly coherent (pure) and a fully incoherent (completely mixed) electron distribution, modeling the density matrix ρ_{in} of photoelectrons generated, for example, by UV illumination of a solid target. These states are then made to interact with a traveling plasmon polariton excited by a mid-IR (MIR) optical field with a photon energy significantly smaller than the energy width of the photoemitted electrons. The MIR and UV pulses are considered mutually phase-locked (e.g., via harmonics generation), so that the electron, if photoemitted in a pure state by carrying phase information imprinted from the UV light, is also phase-locked to the MIR light. First, we consider electrons emitted in a pure Gaussian state (Fig. 5, A and B, and see Materials and Methods for details) for which the coherent interaction with the SPP field results in a generally asymmetric spectrogram, whose shape strongly depends on the phase difference between the SPP field and the UV photon used in the photoemission process. We stress that this phase dependence is a general property of any pure state spectrogram, while the asymmetry is not necessarily observed and might be absent for some particular profiles of the wave functions. In contrast, when considering the spectrogram of a completely mixed Gaussian state (Fig. 5, C and D), we find it to be symmetric and phase independent. Thus, by observing the spatial dependence of the electron energy distribution, we can establish whether there is partial coherence in the photoemitted electrons.

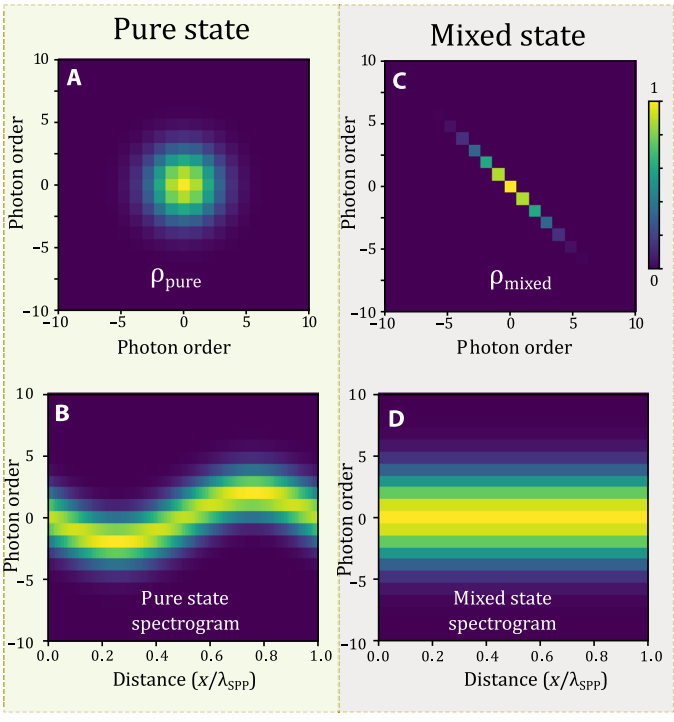

Fig. 5. Proposal for the determination of the coherence of photoemitted electrons. (**A**) Density matrix of a fully coherent (pure) state created by photoemission. (**B**) Spatially dependent spectrogram formed after interaction of the pure state with an SPP. (**C**) Density matrix of the completely mixed state. (**D**) Spectrogram formed after interaction of the mixed state with an SPP.

This observation allows us to propose a further extension of the UEM holographic imaging discussed above. Figure 5B suggests that the spectrogram formed by coherent photoelectrons encodes information about the spatial phase distribution of SPPs, even without making use of the reference optical field, thus providing the most practical realization of quantum holographic UEM.

Similar to the approach described by Priebe *et al.* (*47*), our methods also provide sufficient information for the reconstruction of the complete density matrix of an unknown electronic state, but now, in contrast to their approach, which consists in obtaining the density matrix after multiple acquisitions with different phase or amplitude field configurations, our scheme uses well-controlled spatially dependent SPP fields to realize a number of projective measurements in a parallel fashion. Besides purely practical aspects, the intrinsically parallel nature of the acquisition method can be interesting in evaluating entanglement between single electrons. The position-dependent unitary interaction not only allows us to project the electron state onto different measurement bases, which is a necessary tool for revealing entanglement, but also allows us to simultaneously do it for different electrons. This can be achieved using engineered apertures that direct entangled electrons through the desired regions of the optical field. In addition, coincident detection of the spectrum of entangled electrons, directly applicable to our parallelized scheme, makes it possible to implement a Bell-type experiment for electrons.

CONCLUSIONS

In this work, we have demonstrated both local and spatially separated holographic approaches based on ultrafast transmission electron microscopy. We have shown that these methods significantly improve time resolution. In addition, because they are phase sensitive, they allow us to determine the phase and group velocities of the propagating SPPs involved in the experiment. Moreover, the nonlocal character of our method allows us to completely decouple the reference and probe fields, which is not possible when relying on near-field optical or photoemission microscopy techniques. We remark that our demonstration of spatially separated quantum holography is enabled by exploiting the interaction with a semi-infinite light field, which provides a nearly perfect material-independent reference. The extension of this method to any local collective field promoting periodic modulation of the electron wave function is straightforward and offers a unique perspective

to achieve atomic and subfemtosecond combined resolution in transmission electron microscope (TEM). Possible objects of interest to be studied with this technique are atomic polarizabilities, excitons, phonons, Higgs, and other collective and quasiparticle excitations in condensed matter systems. In addition, our method enables a spatially resolved detection method of coherences in electron quantum states with great potential for electron quantum optics applications.

MATERIALS AND METHODS

Experimental

Electron-transparent samples were prepared by depositing through sputtering a silver thin film (43 nm) on a Si_3N_4 membrane (30 nm) suspended on an 80 μm by 80 μm window in a Si support. Grooves completely penetrating the Ag film and partially penetrating the Si_3N_4 membrane were produced by focused Ga ion beam milling. The samples were mounted in a double-tilt TEM holder.

The 55-fs-long, 1.57-eV, 300-kHz repetition rate optical pulses from a Ti:Sapphire regenerative amplifier were used as both signal and reference fields. The third harmonic of these pulses was used to produce electron pulses via photoemission from a LaB_6 cathode. Experiments were conducted in a modified JEOL-2100 TEM, as described in (*48*).

In all of our experiments, the full width at half maximum of the laser beams was 25 μm. For the local holography experiment, SPPs were selectively excited by aligning the laser polarization with the normal-to-edge direction; this was achieved by maximizing the PINEM response from a single pulse in the region of the sample where excitation only from one nanocavity was present. Energy-filtered imaging was performed using a Gatan GIF Quantum electron energy loss spectrometer.

In our experimental setup, the light beam propagated at an angle of 4.5° ± 1° with respect to the direction of the electron beam, which was oriented along the optical axis of the microscope. For the local interference experiment, the sample was tilted by 12° with respect to electron direction while maintaining the normal to the surface within the plane defined by the light and electron beam directions. This allowed us to minimize the contribution from the semi-infinite field reflected by the flat sample surface, as, for these conditions, modification produced on the electron wave function by the incident and reflected beams was exactly canceled (*35*). The presence of this tilt resulted in retardation effects, which were manifested as a tilt of the plasmon wavefront with respect to the edge of the groove sources. The images presented in Figs. 2 and 4 are projections of the electron distribution on the plane perpendicular to the optical axis of the microscope. Geometrical considerations accounting for the retardation effects and the calculation of the corresponding corrections to the phase and group velocities are presented in note S1.

Data analysis

The data presented in Figs. 2 and 4 were acquired in the zero-loss peak suppression mode described in (*26*). To make the contrast more visible, we subtracted a slowly varying background in Fig. 2, approximated by a 2D parabolic function and originating predominantly in the beam shape and a nonholographic PINEM offset. The magnification of the images was calibrated with a 463-nm optical replica calibration sample. Presented images were median-filtered to remove off-scale pixels produced by cosmic rays. The theoretical estimates of group and phase velocities were conducted as described in (*25*).

Calculation of the electron spectra

The electron energy spectra shown in Fig. 3A were calculated as described in (*35*) for electron and photon pulses of 60 fs and under a tilt angle of θ = 35°. The intensity of both reference and signal fields was taken to be 0.13 GW/cm^2.

Calculation of the spectrograms for the pure and mixed electronic states

Two extreme types of electronic quantum states were considered as input of the holographic technique considered in Fig. 5: a pure (p) Gaussian state with wave function $|\psi\rangle_p = \sum_i g(E_i)|E_i\rangle$, where $g(E_i)$ is a Gaussian probability amplitude, and a completely mixed (cm) Gaussian state with a diagonal density matrix $\rho_{cm} = \sum_i h(E_i)|E_i\rangle\langle E_i|$, where $h(E_i)$ is a Gaussian probability. In the interaction picture, the two optical interactions implemented in the spatially separated holographic method are described by the unitary operators (*31*, *38*, *40*, *47*) $U_1 = e^{\beta_1 a^\dagger - \beta_1^* a}$ and $U_2(x) = e^{\beta_2(x) a^\dagger - \beta_2(x)^* a}$, where β_1 and $\beta_2(x)$ are complex coupling constants determined by the field amplitudes, while a and $a^\dagger$ are commutation operators that lower and raise the number of electron-photon exchanges. Notice that β_1 is uniform over the sample plane, as it is determined by the reflection of the normally incident light, whereas $\beta_2(x)$ shows a space dependence originating in the phase accumulated during plasmon propagation.

The initial states evolve into

$$\rho_{out}(x) = U_2(x)U_1\rho {U_1}^\dagger U_2(x)^\dagger = U_{tot}\rho {U_{tot}}^\dagger$$

where $U_{tot} = U_2(x)U_1 = e^{\beta_{tot} a^\dagger - \beta_{tot}^* a}$ with $\beta_{tot} = \beta_1 + \beta_2(x)$.

The calculations shown in Fig. 5 are obtained by taking $\beta_1 = 0$ and $\beta_2(x) = Ae^{i\Delta\varphi}e^{ikx}$, where A and k are set to 5 and 1, respectively, and $\Delta\varphi$ is the phase difference between the laser pulses used for photoemission and SPP generation. In the absence of the first interaction, we demonstrated the possibility of performing holography with coherent electrons, without making use of the reference field.

SUPPLEMENTARY MATERIALS

Supplementary material for this article is available at http://advances.sciencemag.org/cgi/content/full/5/5/eaav8358/DC1

Note S1. Calculation of group and phase velocities.

Fig. S1. Wavefronts of the plasmons forming the interference pattern for arbitrary light wavefront tilt (incidence direction in the sample plane).

Movie S1. Plasmon hologram evolution with 0.33-fs time step.

Movie S2. Plasmon hologram evolution over 145-fs delay span.

REFERENCES AND NOTES

1. D. Gabor, A new microscopic principle. *Nature* **161**, 777–778 (1948).
2. D. Gabor, Microscopy by reconstructed wave-fronts. *Proc. Royal Soc. Lond.* **197**, 454–487 (1949).
3. M. E. Haine, T. Mulvey, The formation of the diffraction image with electrons in the gabor diffraction microscope. *J. Opt. Soc. Am.* **42**, 763–773 (1952).
4. B. Javidi, T. Nomura, Securing information by use of digital holography. *Opt. Lett.* **25**, 28–30 (2000).
5. B. Javidi, A. Carnicer, M. Yamaguchi, T. Nomura, E. Pérez-Cabré, M. S. Millán, N. K. Nishchal, R. Torroba, J. F. Barrera, W. He, X. Peng, A. Stern, Y. Rivenson, A. Alfalou, C. Brosseau, C. Guo, J. T. Sheridan, G. Situ, M. Naruse, T. Matsumoto, I. Juvells, E. Tajahuerce, J. Lancis, W. Chen, X. Chen, P. W. H. Pinkse, A. P. Mosk, A. Markman, Roadmap on optical security. *J. Opt.* **18**, 083001 (2016).
6. W. Xu, M. H. Jericho, I. A. Meinertzhagen, H. J. Kreuzer, Digital in-line holography for biological applications. *Proc. Natl. Acad. Sci. U.S.A.* **98**, 11301–11305 (2001).
7. H. Lichte, M. Lehmann, Electron holography—Basics and applications. *Rep. Prog. Phys.* **71**, 016102 (2008).

8. A. Tonomura, Applications of electron holography. *Rev. Mod. Phys.* **59**, 639–669 (1987).
9. P. A. Midgley, R. E. Dunin-Borkowski, Electron tomography and holography in materials science. *Nat. Mater.* **8**, 271–280 (2009).
10. W. D. Rau, P. Schwander, F. H. Baumann, W. Höppner, A. Ourmazd, Two-dimensional mapping of the electrostatic potential in transistors by electron holography. *Phys. Rev. Lett.* **82**, 2614–2617 (1999).
11. C. Gatel, A. Lubk, G. Pozzi, E. Snoeck, M. Hÿtch, Counting elementary charges on nanoparticles by electron holography. *Phys. Rev. Lett.* **111**, 025501 (2013).
12. R. E. Dunin-Borkowski, M. R. McCartney, R. B. Frankel, D. A. Bazylinski, M. Posfai, P. R. Buseck, Magnetic microstructure of magnetotactic bacteria by electron holography. *Science* **282**, 1868–1870 (1998).
13. J. D. Maynard, E. G. Williams, Y. Lee, Nearfield acoustic holography: I. Theory of generalized holography and the development of NAH. *J. Acoust. Soc. Am.* **78**, 1395–1413 (1985).
14. S. Eisebitt, J. Lüning, W. F. Schlotter, M. Lörgen, O. Hellwig, W. Eberhardt, J. Stöhr, Lensless imaging of magnetic nanostructures by x-ray. *Nature.* **432**, 885–888 (2004).
15. A. M. Weiner, D. E. Leaird, D. H. Reitze, E. G. Paek, Spectral holography of shaped femtosecond pulses. *Opt. Lett.* **17**, 224–226 (1992).
16. T. Balciunas, A. Melninkaitis, G. Tamosauskas, V. Sirutkaitis, Time-resolved off-axis digital holography for characterization of ultrafast phenomena in water. *Opt. Lett.* **33**, 58–60 (2008).
17. A. Rebane, J. Feinberg, Time-resolved holography. *Nature* **351**, 378–380 (1991).
18. A. Kubo, K. Onda, H. Petek, Z. Sun, Y. S. Jung, H. K. Kim, Femtosecond imaging of surface plasmon dynamics. *Nano Lett.* **5**, 1123–1127 (2005).
19. M. Dąbrowski, Y. Dai, H. Petek, Ultrafast microscopy: Imaging light with photoelectrons on the nano–femto scale. *J. Phys. Chem. Lett.* **8**, 4446–4455 (2017).
20. V. Migunov, C. Dwyer, C. B. Boothroyd, G. Pozzi, R. E. Dunin-Borkowski, Prospects for quantitative and time-resolved double and continuous exposure off-axis electron holography. *Ultramicroscopy* **178**, 48–61 (2017).
21. T. Niermann, M. Lehmann, T. Wagner, Gated interference for time-resolved electron holography. *Ultramicroscopy* **182**, 54–61 (2017).
22. G. M. Vanacore, A. W. P. Fitzpatrick, A. H. Zewail, Four-dimensional electron microscopy: Ultrafast imaging, diffraction and spectroscopy in materials science and biology. *Nano Today* **11**, 228–249 (2016).
23. A. Feist, N. Bach, N. Rubiano da Silva, T. Danz, M. Möller, K. E. Priebe, T. Domröse, J. G. Gatzmann, S. Rost, J. Schauss, S. Strauch, R. Bormann, M. Sivis, S. Schäfer, C. Ropers, Ultrafast transmission electron microscopy using a laser-driven field emitter: Femtosecond resolution with a high coherence electron beam. *Ultramicroscopy* **176**, 63–73 (2017).
24. B. Barwick, D. J. Flannigan, A. H. Zewail, Photon-induced near-field electron microscopy. *Nature* **462**, 902–906 (2009).
25. T. T. A. Lummen, R. J. Lamb, G. Berruto, T. LaGrange, L. Dal Negro, F. J. García de Abajo, D. McGrouther, B. Barwick, F. Carbone, Imaging and controlling plasmonic interference fields at buried interfaces. *Nat. Commun.* **7**, 13156 (2016).
26. E. Pomarico, I. Madan, G. Berruto, G. M. Vanacore, K. Wang, I. Kaminer, F. J. García de Abajo, F. Carbone, meV resolution in laser-assisted energy-filtered transmission electron microscopy. *ACS Photonics.* **5**, 759–764 (2018).
27. A. J. McKenna, J. K. Eliason, D. J. Flannigan, Spatiotemporal evolution of coherent elastic strain waves in a single MoS_2 flake. *Nano Lett.* **17**, 3952–3958 (2017).
28. G. Berruto, I. Madan, Y. Murooka, G. M. Vanacore, E. Pomarico, J. Rajeswari, R. Lamb, P. Huang, A. J. Kruchkov, Y. Togawa, T. LaGrange, D. McGrouther, H. M. Rønnow, F. Carbone, Laser-induced skyrmion writing and erasing in an ultrafast cryo-Lorentz transmission electron microscope. *Phys. Rev. Lett.* **120**, 117201 (2018).
29. N. Rubiano da Silva, M. Möller, A. Feist, H. Ulrichs, C. Ropers, S. Schäfer, Nanoscale mapping of ultrafast magnetization dynamics with femtosecond Lorentz microscopy. *Phys. Rev. X.* **8**, 031052 (2018).
30. F. Houdellier, G. M. Caruso, S. Weber, M. Kociak, A. Arbouet, Development of a high brightness ultrafast transmission electron microscope based on a laser-driven cold field emission source. *Ultramicroscopy* **186**, 128–138 (2018).
31. K. E. Echternkamp, A. Feist, S. Schäfer, C. Ropers, Ramsey-type phase control of free-electron beams. *Nat. Phys.* **12**, 1000–1004 (2016).
32. L. Piazza, T. T. A. Lummen, E. Quiñonez, Y. Murooka, B. W. Reed, B. Barwick, F. Carbone, Simultaneous observation of the quantization and the interference pattern of a plasmonic near-field. *Nat. Commun.* **6**, 6407 (2015).
33. S. T. Park, M. Lin, A. H. Zewail, Photon-induced near-field electron microscopy (PINEM): Theoretical and experimental. *New J. Phys.* **12**, 123028 (2010).
34. M. T. Hassan, J. S. Baskin, B. Liao, A. H. Zewail, High-temporal-resolution electron microscopy for imaging ultrafast electron dynamics. *Nat. Photonics* **11**, 425–430 (2017).
35. K. Wang, E. Pomarico, R. J. Lamb, D. McGrouther, I. Kaminer, B. Barwick, F. J. García de Abajo, F. Carbone, Attosecond coherent control of free-electron wave functions using semi-infinite light fields. *Nat. Commun.* **9**, 2694 (2018).
36. F. J. García De Abajo, Optical excitations in electron microscopy. *Rev. Mod. Phys.* **82**, 209–275 (2010).
37. F. O. Kirchner, A. Gliserin, F. Krausz, P. Baum, Laser streaking of free electrons at 25 keV. *Nat. Photonics* **8**, 52–57 (2013).
38. A. Feist, K. E. Echternkamp, J. Schauss, S. V. Yalunin, S. Schäfer, C. Ropers, Quantum coherent optical phase modulation in an ultrafast transmission electron microscope. *Nature* **521**, 200–203 (2015).
39. T. Plettner, R. L. Byer, T. I. Smith, E. Colby, B. Cowan, C. M. S. Sears, J. E. Spencer, R. H. Siemann, First observation of laser-driven acceleration of relativistic electrons in a semi-infinite vacuum space. *Proc. IEEE Part. Accel. Conf.* **2005**, 650–652 (2005).
40. F. J. García de Abajo, B. Barwick, F. Carbone, Electron diffraction by plasmon waves. *Phys. Rev. B.* **94**, 041404 (2016).
41. L. Yin, V. K. Vlasko-Vlasov, A. Rydh, J. Pearson, U. Welp, S.-H. Chang, S. K. Gray, G. C. Schatz, D. B. Brown, C. W. Kimball, Surface plasmons at single nanoholes in Au films. *Appl. Phys. Lett.* **85**, 467–469 (2004).
42. V. S. Yakovlev, J. Gagnon, N. Karpowicz, F. Krausz, Attosecond streaking enables the measurement of quantum phase. *Phys. Rev. Lett.* **105**, 073001 (2010).
43. M. Wollenhaupt, A. Assion, D. Liese, C. Sarpe-Tudoran, T. Baumert, S. Zamith, M. A. Bouchene, B. Girard, A. Flettner, U. Weichmann, G. Gerber, Interferences of ultrashort free electron wave packets. *Phys. Rev. Lett.* **89**, 173001 (2002).
44. W. A. Okell, T. Witting, D. Fabris, C. A. Arrell, J. Hengster, S. Ibrahimkutty, A. Seiler, M. Barthelmess, S. Stankov, D. Y. Lei, Y. Sonnefraud, M. Rahmani, T. Uphues, S. A. Maier, J. P. Marangos, J. W. G. Tisch, Temporal broadening of attosecond photoelectron wavepackets from solid surfaces. *Optica* **2**, 383 (2015).
45. Y. Mairesse, F. Quéré, Frequency-resolved optical gating for complete reconstruction of attosecond bursts. *Phys. Rev. A* **71**, 011401 (2005).
46. C. Bourassin-Bouchet, M.-E. Couprie, Partially coherent ultrafast spectrography. *Nat. Commun.* **6**, 6465 (2015).
47. K. E. Priebe, C. Rathje, S. V. Yalunin, T. Hohage, A. Feist, S. Schäfer, C. Ropers, Attosecond electron pulse trains and quantum state reconstruction in ultrafast transmission electron microscopy. *Nat. Photonics* **11**, 793–797 (2017).
48. L. Piazza, D. J. Masiel, T. LaGrange, B. W. Reed, B. Barwick, F. Carbone, Design and implementation of a fs-resolved transmission electron microscope based on thermionic gun technology. *Chem. Phys.* **423**, 79–84 (2013).

Acknowledgments: We thank I. Kaminer (Faculty of Electrical Engineering and Solid State Institute, Technion, Haifa, Israel) and M. Hassan (Department of Physics, University of Arizona, Tucson, USA) for fruitful discussions. **Funding:** The LUMES laboratory acknowledges support from the NCCR MUST. G.B. acknowledges financial support from the Swiss National Science Foundation (SNSF) through the grant no. 200021_159219/1. E.P. acknowledges financial support from the SNSF through an Advanced Postdoc Mobility grant no. P300P2_158473. F.J.G.d.A. acknowledges support from the Spanish MINECO (MAT2017-88492-R and SEV2015-0522), the European Research Council (Advanced ERC grant no. 789104-eNANO), and Cellex Foundation. **Author contributions:** T.T.A.L. designed the sample geometry. R.J.L. and D.M. fabricated the sample. I.M., G.M.V., and G.B. conducted experiments. G.M.V. and I.M. analyzed data. E.P. performed calculations. I.M., E.P., G.M.V., G.B., F.J.G.d.A., and F.C. interpreted results. I.M., E.P., G.M.V., G.B., T.L., F.J.G.d.A., and F.C. contributed to writing the article. **Competing interests:** The authors declare that they have no competing interests. **Data and materials availability:** All data needed to evaluate the conclusions in the paper are present in the paper and/or the Supplementary Materials. Additional data related to this paper may be requested from the authors.

Submitted 25 October 2018
Accepted 15 March 2019
Published 3 May 2019
10.1126/sciadv.aav8358

Citation: I. Madan, G. M. Vanacore, E. Pomarico, G. Berruto, R. J. Lamb, D. McGrouther, T. T. A. Lummen, T. Latychevskaia, F. J. García de Abajo, F. Carbone, Holographic imaging of electromagnetic fields via electron-light quantum interference. *Sci. Adv.* **5**, eaav8358 (2019).